University of Bath

Computational Studies of a Novel Magnetically Driven Single-Use-Technology Bioreactor: A Comparison of Mass Transfer Models

Richard Maltby[a,b], Shuai Tian[b], Y.M. John Chew[a,b]*

[a]*Centre for Sustainable Chemical Technologies, University of Bath, Bath, BA2 7AY, UK.*

[b]*Centre for Advanced Separations Engineering, Department of Chemical Engineering, University of Bath, Bath, BA2 7AY, UK.*

* corresponding author: y.m.chew@bath.ac.uk

Abstract

This work applies computational fluid dynamics (CFD) modelling to a novel 1,000 litre design of single-use-technology (SUT) bioreactor, with a magnetically driven floor-mounted impeller and spargers distributed across the tank floor. A two-phase Euler-Euler model using the k-ε turbulence model and population balance is presented alongside the use of immersed solid method for modelling the impeller motion. This work also provides the first CFD analysis of a large-scale SUT bioreactor, identifying key flow characteristics of the non-standard design at different operating conditions. Five models for the mass transfer coefficient, k_L, are compared, with $k_L a$ values compared to experimental measurements. The slip velocity model is found to be the best prediction of the mass transfer coefficient for this SUT system. Separating the influence of the mass transfer coefficient and specific area, a, shows that the latter is the dominant driving force behind changes in $k_L a$ that occur at different operating conditions. Comparing the present work to previous studies for traditional stirred tanks highlights the need for understanding the hydrodynamics of non-standard reactor designs when identifying suitable mass transfer models in gas-liquid flow systems.

Keywords

Single-Use-Technologies; Bioreactor; CFD; Mass Transfer; Immersed Solid

1. Introduction

Single-Use-Technology (SUT) reactors are a class of disposable bioprocessing equipment used mainly in the biopharmaceutical industry, where pre-sterilised plastic components are disposed of and replaced after use. The popularity and range of available SUT processes and equipment has increased in recent years, primarily in the biopharmaceuticals industry [1]. SUT bioreactors provide a viable alternative to traditional stainless steel bioreactors, and can be categorised by agitation mechanism as rocking (up to 500 L scale) or stirred type (up to 2,000 L scale) [2]. Benefits of the adoption of SUT concepts in production processes include reduced cross-contamination and assured sterility, flexibility, financial, productivity and environmental considerations. The use of SUT bioreactors largely eliminates the need for sterilisation and cleaning between processes, with the manufacturer of a 100 L wave-type SUT bioreactor claiming a reduction in turnaround time from 8-10 hours for a traditional stainless steel technologies to just 1-2 hours [3]. Furthermore, a similar turnaround time is claimed between different products, significantly increasing the flexibility of a process whilst simultaneously reducing downtime and labour requirements. It has also been reported that significant cost savings can be made by adopting SUT processes. This takes the form of reduced capital costs through reduced equipment purchase costs and shorter build times, and reduced operating costs, largely through reduced cleaning and labour requirements. A lifecycle analysis approach by Pietrzykowski *et al* [4] has shown that the overall environmental impact of an SUT facility can be significantly lower than comparable stainless steel processes, with the greatest improvements coming from water and energy use due to cleaning. However, using SUT components does lead to an increase in plastic waste generation of up to 455% for a fully SUT facility [1], which will increase the consumables requirement and requires appropriate disposal.

There is a range of currently available stirred SUT bioreactors with varying production capacity [1], however these have been largely limited to applications in the production of high-value products from mammalian [5], and less commonly plant cells [6]. This leaves the wider industrial

biotechnology sector largely untouched by SUT concepts, with only small-scale microbial investigations reported [7]. There is also a lack of industry standardisation, with the supply chain often tied to the fate of a single component supplier [1], however this also gives the option to tailor the equipment and sparger design to a particular process need to a degree that is not generally possible with traditional stainless steel bioprocessing equipment.

The use of CFD modelling as a tool for assessing the flow in stirred tanks is a field which has been developing since the mid-1980s with the single-phase models of Harvey and Greaves [8,9]. Since then, the complexity of the models has increased alongside an increase in available computing power, with more complex impeller motion and turbulence models amongst the most significant developments. The modelling of two-phase gas-liquid systems first became feasible in 2D in the mid-1990s, with the development of Euler-Euler methods, with 3D simulations developing during the early 2000s using a range of different interfacial drag and population balance models applied. A thorough analysis of the development of single and two-phase modelling in stirred tanks is reported in the review series of Joshi *et al* [10,11]. Within the published body of work surrounding stirred tank modelling, a wide range of different shaft-driven impeller and baffle geometries have been used. However, there is a lack of analysis of non-cylindrical reactor designs and magnetically stirred tanks.

Oxygen transfer in bioreactors and fermenters is a very important characteristic, as dissolved oxygen can become the limiting factor in processes with high oxygen demand such as some bacterial fermentations. It is routinely reported in terms of the combined value $k_L a$, which can be easily measured experimentally from dissolved oxygen measurements using various techniques [12,13], both with and without the presence of biomass. Separating the terms k_L and a is difficult experimentally, however it is an approach commonly used in CFD modelling to describe the mass transfer in two-phase systems. The two most commonly used models for the study of mass transfer in gas-liquid flows are the penetration and eddy cell models, which both take the form of equation 1.

For the ease of comparison, models of this form will be referred to collectively as the eddy model. The penetration model is based on Higbie's penetration theory of interfacial transfer [14], with the assumption that the contact time can be approximated by the Kolmogorov length scale due to the influence of small eddies on the mass transfer. In contrast, the eddy cell model was derived by Lamont and Scott [15] by modelling the mass transfer into idealised eddies of sizes across the energy scale, giving a theoretically derived proportionality constant of 0.4.

$$k_L = K \sqrt{D_L \sqrt{\frac{\varepsilon}{v}}}$$

(1)

where k_L = volumetric mass transfer coefficient, K = proportionality constant, D_L = diffusivity, ε = turbulence dissipation, v = kinematic viscosity

Other values of this proportionality constant have also been applied to CFD simulations including the frequently applied value of 0.301 proposed by Kawase *et al* [16]*.* Other constants are based on fitting this form of the equation to empirical values, including 0.523 [17] and 0.592 [18] and 0.7 [19].

Another model applied to stirred tank studies is the slip velocity model, which is a variation on penetration theory where the contact time for the liquid at the bubble surface is assumed to be dependent on the slip velocity, v_b, between the phases [14].

$$k_L = \frac{2}{\sqrt{\pi}} \sqrt{\frac{D_L v_b}{d_b}}$$

(2)

where v_b = slip velocity, d_b = bubble diameter.

The mass transfer coefficient can also be calculated by considering the Sherwood number. Alves [20] proposed a model based on a simplification of the Frössling correlation [21], which is referred to as a 'rigid' model due to the assumption that the bubbles are sufficiently rigid that the correlations developed for spherical particles are applicable. It is also assumed that the influence of forced convection is much greater than natural convection, meaning that the coefficient of 2 can be neglected in equation 3.

$$Sh = \frac{k_L d_b}{D_L} = 2 + 0.6 Re^{1/2} Sc^{1/3} \qquad (3)$$

where Sh = Sherwood number, Re = Reynolds number, Sc = Schmidt number.

A final mass transfer model that is considered applicable to CFD models, but is as yet unused as such, is presented by Jajuee et al [22], which combines aspects of surface renewal and penetration theory. It has been correlated against experimental with a high degree of accuracy claimed [22].

The mass transfer coefficient k_L is multiplied by the specific interfacial area between the gas and liquid phases, a, calculated using equation 4, to give the value of $k_L a$.

$$a = \frac{6 \alpha_g}{d_b} \qquad (4)$$

where α_g = gas volume fraction.

A summary of the CFD studies for stirred-tank systems including interphase mass transfer is presented in Table 1. The eddy model, with constants ranging from 0.3 to 1.13, is the most widely applied form of mass transfer model applied in previous CFD studies (see Table 1). A limited number

of comparative studies between different mass transfer models are also included in Table 1. A CFD model with population balance was used for the comparison of four different mass transfer models for a multi-impeller stirred reactor presented by Ranganathan and Sivaraman [23]. Comparing to experimental data [20], the eddy cell model was shown to provide the best fit to $k_L a$ values out of the models proposed. Gimbun *et al* [24] found the slip velocity and eddy cell methods to be in good agreement for stirred tank models at the 14 and 200 L scale, with the larger $k_L a$ values predicted using the slip velocity model, whereas Appa *et al* [19] found the eddy cell model in combination with a population balance to provide the best fit to experimental data.

The same approaches to modelling $k_L a$ in two-phase CFD models has also been applied to bubbly flows in bubble columns (i.e. with no stirring), including the eddy model with a proportionality constant of $2/\sqrt{\pi}$ [31] and the slip velocity Model [32–35]. There has also been reported success for bubble column modelling using constant values of k_L [36,37]. This analysis shows that there is no consensus in literature on the most appropriate form of the mass transfer coefficient to be used in conjunction with the two-phase CFD modelling of bubbly flows. Furthermore, there has been a very wide range of proportionality constants, both theoretically and empirically derived, applied for the eddy model, which is the most commonly applied model for k_L.

This work aims to characterise the mass transfer and hydrodynamics in a novel 1,000 L SUT bioreactor, based on a cubic design with floor-mounted magnetic stirring and distributed gas sparging, designed to be compatible with a wide range of industrially significant fermentation processes. This is the first time that a CFD modelling approach has been applied to large-scale SUT equipment, and will further improve the understanding of mixing and mass transfer in such equipment. A comparison between different mass transfer models proposed in literature will be made, comparing to experimental data, with the relative accuracy of each model assessed against previous studies in conventional two-phase stirred tanks.

Table 1: CFD studies of stirred tanks including interphase mass transfer. K = proportionality constant.

Author(s)	Year	Mass Transfer Model(s)
Bakker and Van den Akker [25]	1994	Eddy Model (K = 0.301)
Laakkonen et al [26]	2006	Eddy Model (K = 0.301)
Gimbun et al [24]	2009	Eddy Model (K = 0.4), Slip Velocity Model
Kerdouss et al [27]	2008	Eddy Model (K = $2/\sqrt{\pi}$)
Moilanen et al [28]	2008	Eddy Model (K = 0.3)
Zhang et al [29]	2009	Eddy Model (K = $2/\sqrt{\pi}$)
Ranganathan and Sivaraman [23]	2011	Eddy Model (K = 0.4 & $2/\sqrt{\pi}$), Slip Velocity Model, Rigid Model
Buffo et al [30]	2012	Eddy Model (K = 0.4)
Appa et al [19]	2014	Eddy Model (K = 0.7), Slip Velocity Model

2. Numerical Modelling

2.1 Governing Equations

CFD modelling was performed in the Euler-Euler reference frame using the commercial software

ANSYS CFX 17. The continuity and momentum equations (5-6) for each phase (k = g,l) are used as a

basis for the calculations.

$$\frac{\partial}{\partial t}(\alpha_k \rho_k) + \nabla \cdot (\alpha_k \rho_k \boldsymbol{u}_k) = 0 \tag{5}$$

$$\frac{\partial}{\partial t}(\alpha_k \rho_k \boldsymbol{u}_k) + \nabla \cdot (\alpha_k(\rho_k \boldsymbol{u}_k \otimes \boldsymbol{u}_k)) = -\alpha_k \nabla P' + \nabla \cdot \left(\alpha_k \mu_{eff,k}(\nabla \boldsymbol{u}_k + \nabla \boldsymbol{u}_k{}^T)\right) + \alpha_k(\rho_k - \rho_l)\boldsymbol{g} +$$

$$D_{g,l} + F^{TD}{}_k + S_k \tag{6}$$

where α = volume fraction, ρ = density, $\boldsymbol{u}$ = velocity vector, P' = modified pressure, μ_{eff} = effective

viscosity, $\boldsymbol{g}$ = gravitational vector, $D_{g,l}$ = interphase drag force, F^{TD} = turbulent dispersion force, S_k

= momentum source terms.

The shared pressure field for the two phases P' is expressed as,

$$P' = P + \frac{2}{3}\rho k \tag{7}$$

Turbulence in the liquid phase is modelled using the k-ε turbulence model, which uses Reynolds

averaging to separate the fluctuating and mean velocity fields. This model has been widely applied

to and validated for two-phase Euler-Euler modelling in stirred tanks [11], and is suitable for large-

scale CFD problems such as the 1,000 L SUT bioreactor studied in this work. Furthermore, time-

averaging allows for the efficient computation of steady-state flow patterns, in comparison to

alternatives such as the large eddy simulation which yield time-dependent solutions. The following

two equations are solved for the liquid phase,

$$\frac{\partial}{\partial t}(\alpha_l \rho_l k) + \nabla \cdot \left(\alpha_l(\rho_l \boldsymbol{u}_l k) - \left(\mu_l + \frac{\mu_{T,l}}{\sigma_k}\right)\nabla k\right) = \alpha_l\left(\mu_{T,l}(\nabla \boldsymbol{u}_l + \nabla \boldsymbol{u}_l{}^T)\nabla \boldsymbol{u}_l - \rho_l \varepsilon\right) \tag{8}$$

$$\frac{\partial}{\partial t}(\alpha_l \rho_l \varepsilon) + \nabla \cdot \left((\alpha_l \rho_l \boldsymbol{u}_l \varepsilon) - \left(\mu_l + \frac{\mu_{T,l}}{\sigma_\varepsilon}\right)\nabla \varepsilon\right) = \frac{\alpha_l \varepsilon}{k}\left(C_{\varepsilon 1}(\nabla \boldsymbol{u}_l + \nabla \boldsymbol{u}_l{}^T)\nabla \boldsymbol{u}_l - C_{\varepsilon 2}\rho_l \varepsilon\right) \tag{9}$$

where k = turbulent kinetic energy, μ = dynamic viscosity, μ_T = turbulent viscosity, σ_ε, σ_k, $C_{\varepsilon1}$, $C_{\varepsilon2}$ = constants.

The turbulent viscosity, $\mu_{T,l}$, is used as a closure for the turbulence model with constant C_μ. The constants used in this turbulence model are included in Table 2.

$$\mu_{T,l} = \rho_l C_\mu \frac{k^2}{\varepsilon} \tag{10}$$

No turbulence model is applied to the dispersed gas phase, with the gas phase turbulent viscosity, $\mu_{T,g}$, calculated using equation 11.

$$\mu_{T,g} = \frac{\rho_g}{\rho_l} \mu_{T,l} \tag{11}$$

The effective viscosity, μ_{eff}, for the liquid and gas phases is calculated from equations 12-14. The term $\mu_{T,p}$ is an enhancement based on particle induced turbulence [38].

$$\mu_{eff,l} = \mu_l + \mu_{T,l} + \mu_{T,p} \tag{12}$$

$$\mu_{T,p} = 0.6\rho_l \alpha_g d_b |\boldsymbol{u}_g - \boldsymbol{u}_l| \tag{13}$$

$$\mu_{eff,g} = \mu_g + \mu_{T,g} \tag{14}$$

Table 2: Constants used in the k-ε turbulence model

$C_{\varepsilon1}$	$C_{\varepsilon2}$	σ_k	σ_ε	C_μ
1.44	1.92	1.00	1.30	0.09

The interphase drag force, $D_{g,l}$, between the gas bubbles and the liquid phase is calculated using equation 15. Other interphase forces (i.e. lift, wall lubrication and virtual mass) involved in two phase flow are neglected due to the dominance of the drag force in stirred tank systems [20,24].

$$D_{g,l} = \frac{3}{4}\frac{C_D}{d_b}\alpha_g\rho_l|u_g - u_l|(u_g - u_l) \tag{15}$$

The drag coefficient, C_D, is calculated using the Ishii-Zuber model [39], which was developed for densely populated dispersed phase flows since the drag coefficient is modified depending on the local dispersed phase volume fraction. The model accounts for the deformation of larger bubbles and bubbles in regions of dense gas phase, both of which are expected to be present in the studied system. The equations employed to describe the drag coefficient, with mixture Reynolds number Re_m, in the bubbly (spherical), ellipsoidal and spherical cap flow regimes are,

For bubbles in the spherical flow regime:

$$C_D(sphere) = \frac{24}{Re_m}\left(1 + 0.15Re_m^{0.687}\right) \tag{16}$$

$$Re_m = \frac{\rho_l|u_g-u_l|d_b}{\mu_l(1-\alpha_g)^{-2.5\mu_*}} \quad , \quad \mu_* = \frac{\mu_g+0.4\mu_l}{\mu_g+\mu_l} \tag{17}$$

For bubbles in the elliptical flow regime:

$$C_D(ellipse) = \frac{2}{3}\left(\frac{g\Delta\rho d_b^2}{\sigma}\right)^{0.5}E(\alpha) \tag{18}$$

$$E(\alpha) = \frac{(1+17.67f(\alpha)^{6/7})}{18.67f(\alpha)} \quad , \quad f(\alpha) = \frac{(1-\alpha_g)^{0.5}}{(1-\alpha_g)^{-2.5\mu_*}} \tag{19}$$

For bubbles in the spherical cap regime:

$$C_D(cap) = \frac{3}{8}\left(1 - \alpha_g\right)^2 \qquad (20)$$

The bubble regime is determined locally using the following conditional operators;

$$C_D = C_D(sphere) \quad IF \quad C_D(sphere) \geq C_D(ellipse)$$

$$C_D = min\big(C_D(ellipse), C_D(cap)\big) \quad IF \quad C_D(sphere) < C_D(ellipse)$$

The dispersion force generated by turbulence in the liquid phase, F^{TD}, is calculated using the Favre-averaged turbulence dispersion model [40], equation 21. This force models the effect of turbulence in the liquid phase on the gas phase distribution.

$$F^{TD}{}_l = -F^{TD}{}_g = \frac{3}{4}\frac{C_D}{d_b}\alpha_g|u_g - u_l|\frac{\mu_{T,l}}{0.9}\left(\frac{\nabla\alpha_g}{\alpha_g} - \frac{\nabla\alpha_l}{\alpha_l}\right) \qquad (21)$$

2.2 Population Balance Modelling

The distribution of bubble sizes in the dispersed gas phase is predicted using the homogeneous multiple size group (MUSIG) model. The model is based on the population balance described by equation 22.

$$\frac{\partial}{\partial t}n(m,t) + \frac{\partial}{\partial x^i}\big(u^i(m,t)n(m,t)\big) = B_B - D_B + B_C - D_c \qquad (22)$$

The terms on the right hand side of this equation represent the birth (B_B) and death (D_B) of bubble due to bubble breakup and the birth (B_C) and death (D_C) of bubbles through coalescence. These

terms can be calculated using the following equations for the number fraction (n) of particles with

mass (m) at time (t).

$$B_B = \int_m^\infty g(\varepsilon; m)n(\varepsilon, t)d\varepsilon \tag{23}$$

$$D_B = n(m, t) \int_0^m g_g(m; \varepsilon)d\varepsilon \tag{24}$$

$$B_C = \frac{1}{2}\int_0^m Q(m - \varepsilon; \varepsilon)\, n(m - \varepsilon, t)n(m, t)d\varepsilon \tag{25}$$

$$D_C = n(m, t) \int_m^\infty Q(m; \varepsilon)n(\varepsilon, t)\, dt \tag{26}$$

The range of bubble diameters is discretised into N equally spaced groups between the limits d_{min}

and d_{max} as described by equation 27.

$$d_i = d_{min} + \frac{d_{max} - d_{min}}{N}\left(i - \frac{1}{2}\right) \tag{27}$$

The above population balance equations are discretised in order to be calculated for each of the

bubble size groups as described in the ANSYS CFX documentation [41]. In the homogeneous model,

all bubbles within a size group are assumed to share the same velocity field. The break-up and

coalescence of bubbles are modelled using the Luo and Svendsen [42] and Prince and Blanch [43]

models respectively.

The CFD model is solved as a steady state solution, using the high resolution advection scheme and

turbulence numerics implemented in ANSYS CFX 17. A fixed timestep of 0.005 s is used, and

convergence is said to be achieved when the root-mean-square residuals of hydrodynamic and

turbulent properties have reduced below 10^{-4} and the gas fraction in the reactor has stabilised. High

performance parallel computing has been utilised to solve the CFD model: Balena High Performance Computing (HPC) Service at the University of Bath, running 2 nodes (Intel E5-2650 v2) each with 16 partitions and a maximum of 64 GB RAM. Simulation times for the different conditions are in the region of 4×10^6 to 6×10^6 core seconds (35 to 52 hours for 2 nodes) to reach the specified convergence criteria.

2.3 Mass Transfer Modelling

The mass transfer of oxygen from the gas liquid phase can be described using equation 28 [13]. The rate of transfer is proportional to the concentration driving force, with high values of $k_L a$ increasing the rate of oxygen transfer.

$$N_{O_2} = k_L a (C^*_{O_2 l} - C_{O_2 l}) \tag{28}$$

where N_{O_2} = oxygen transfer rate, $C^*_{O_2 l}$ = saturation dissolved oxygen concentration, $C_{O_2 l}$ dissolved oxygen concentration. Five models are considered for the volumetric liquid phase mass transfer coefficient, k_L, in this work as described in section 1. The models can be used with equation 28 to estimate the mass transfer of oxygen from the gas to the liquid phase, however they can also be applied during post-processing since the dependent parameters are compatible with the outputs of the CFD model.

Table 3: Mass transfer equations applied in the CFD model.

Mass Transfer Model	Modelled Equation	Eqn #
Penetration Model [14]	$k_L = \dfrac{2}{\sqrt{\pi}} \sqrt{D_L \sqrt{\dfrac{\varepsilon}{v}}}$	(29)

Eddy Cell Model [15]	$k_L = 0.4 \sqrt{D_L \sqrt{\dfrac{\varepsilon}{\nu}}}$	(30)
Slip Velocity Model [14]	$k_L = \dfrac{2}{\sqrt{\pi}} \sqrt{\dfrac{D_L v_b}{d_b}}$	(31)
Rigid Model [20]	$k_L = 0.6 \left(\dfrac{v_b}{d_b}\right)^{1/2} (D_L)^{3/2} \nu^{-1/6}$	(32)
Surface Renewal Stretch Model [22]	$k_L = \dfrac{2}{\sqrt{\pi}} \sqrt{D_L \sqrt{\dfrac{V_G g}{\nu}}}$	(33)

3. Design of SUT Bioreactor

3.1 Domain Definition

For this SUT reactor, the gas phase is introduced through disposable micro-porous sparger heads at fourteen individual locations, located in two ring on the floor of the vessel as shown in Figure 1. The model is based on a physical reactor design operated by the Centre for Process Innovation (CPI). A volumetric aeration rate of 0.1 vvm is used, with gas equally distributed between each of the spargers. Mixing is provided by a single floor-mounted impeller (Figure 2) at the center of the reactor, which has a diameter approximately six times smaller than the width of the tank. This design allows for the efficient packing and installation of SUT bags with pre-installed impellers. The combination of this stirring method, localized sparging and the cubic tank geometry mean that the hydrodynamics are expected to be significantly different to traditional bioreactor designs. A single instance of rotational symmetry between the tank corners, sparger locations and impeller blades means that one half of the actual geometry is modelled, with rotational periodicity applied at the symmetry plane. The impeller is modelled at an angle of 25° to the periodic boundary to prevent the blades of the impeller interacting with the boundary. It is assumed that any creasing of the polymeric material at the walls or corners of the tank is negligible for the purpose of CFD modelling. The free surface of the liquid phase is modelled using the degassing boundary condition, which

allows only the gas phase to exit the domain. The continuous liquid phase sees the boundary as a free-slip wall and does on leave the boundary. The deformation of the free surface due to bubble breakage is therefore not included in the simulation, hence reducing computational time. The tank walls are modelled as no slip with respect to the liquid phase and free slip with respect to the gas phase.

Impeller motion in modelled using the immersed solid method. This method is not universally applicable to two-phase systems due to limitations in the way that the solid impeller walls interact with the dispersed phase [41]. However, for this SUT geometry the gas phase is introduced at multiple locations distributed throughout the tank, unlike many traditional bioreactor designs where the gas phase is sparged directly into the path of the impeller to promote bubble breakup. The predominant interactions affecting the hydrodynamics of the gas phase in this system are therefore with the liquid phase rather than the solid surface. This method has the advantage over the widely used multiple reference frame (MRF) and sliding mesh (SM) methods in that the rotor and stator overlap, with no domain interface being modelled, improving the mesh quality and reducing the number of mesh elements required. Separate studies (not presented here) showed that the volume averaged $k_L a$ values, calculated using the eddy cell model at 400 RPM and assuming a 1 mm constant bubble size, match to within 1.72% when the same conditions are modelled using the MRF method.
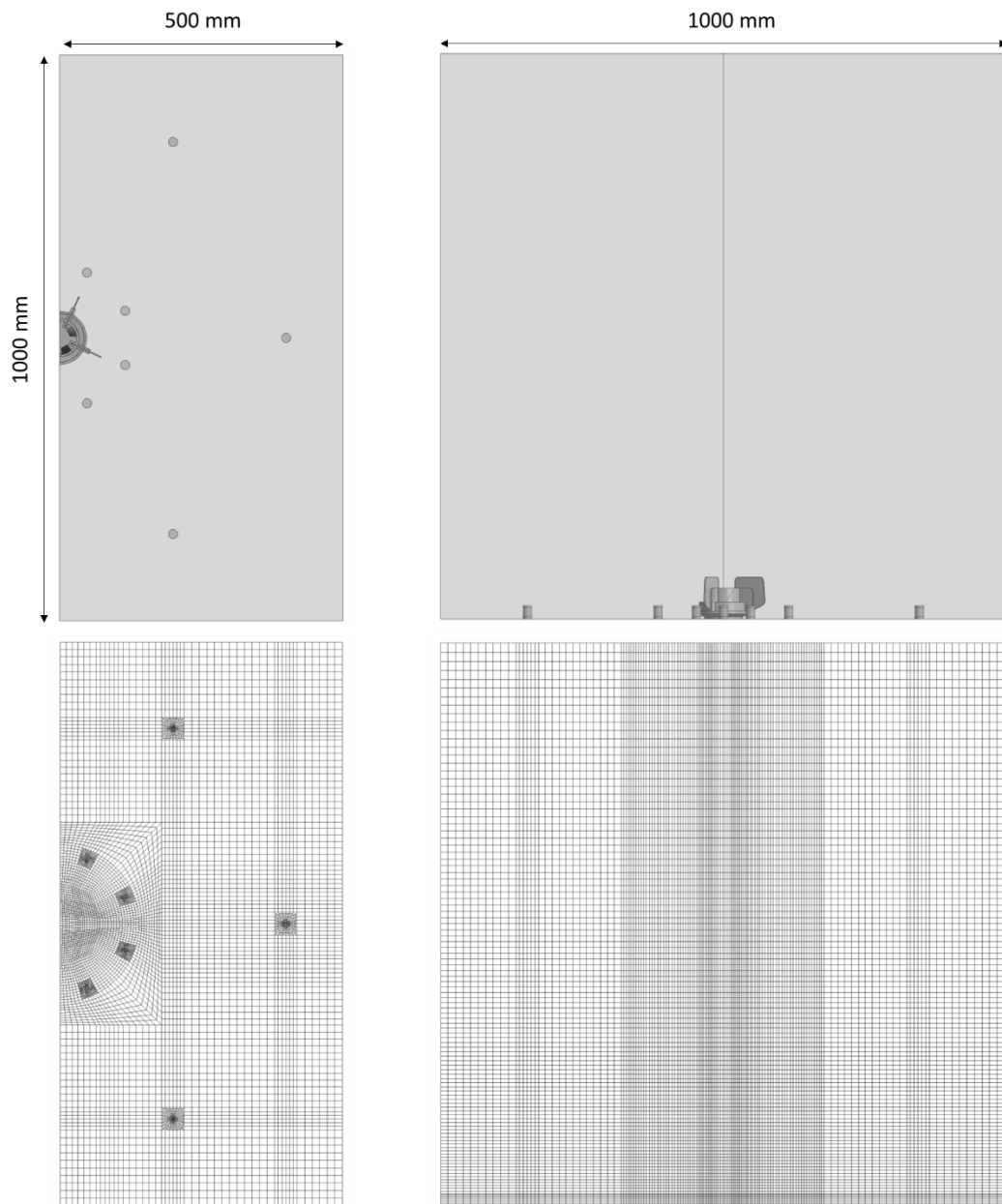
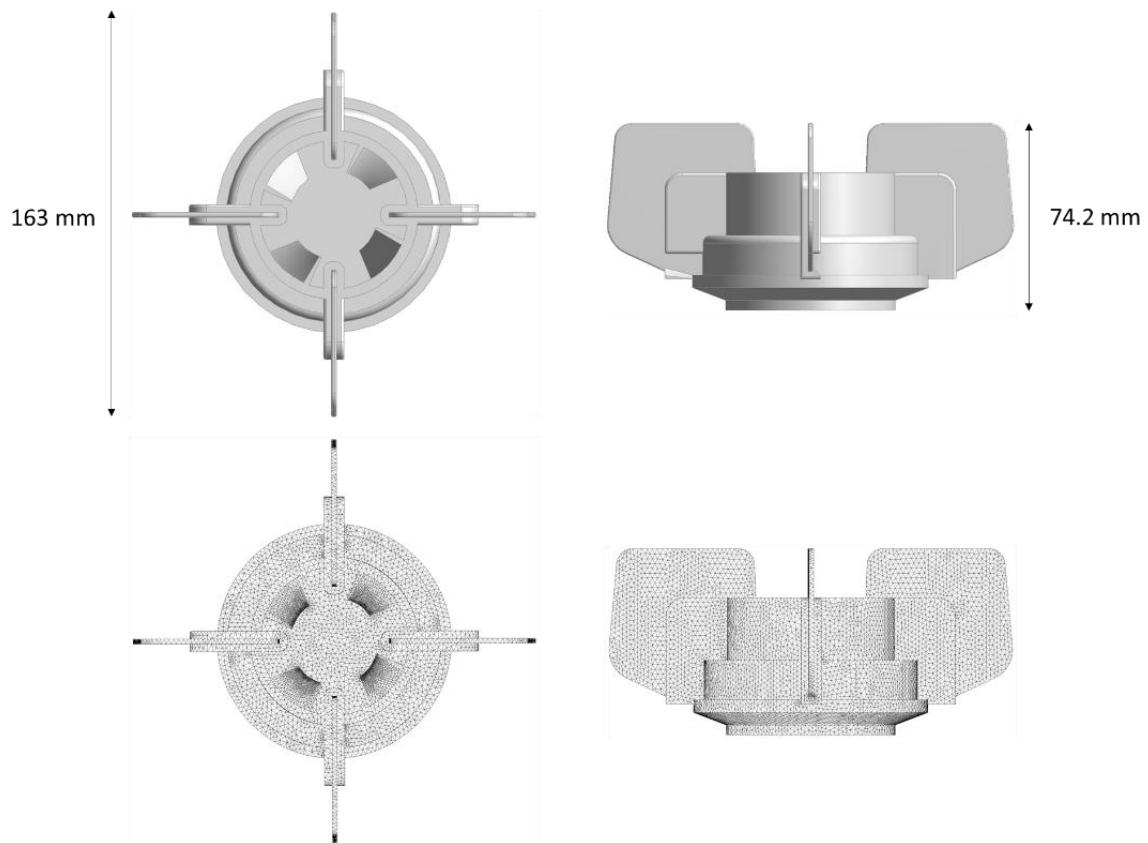Figure 1: Tank geometry (top) and mesh (bottom) for the SUT bioreactor.

Figure 2: Impeller geometry (top) and mesh (bottom) for the SUT bioreactor.

3.2 Mesh Dependency Study

In such a complex system, the influence of the mesh density on the results is usually significant, therefore a mesh dependency study is necessary and was carried out to identify the optimal mesh density for the tank and impeller geometry. Meshing is performed using ANSYS ICEM, producing a structured mesh for the tank (Figure 1) and an unstructured mesh for the complex geometry of the impeller (Figure 2), including mild defeaturing and curvature removal. As shown in Table 4, using the immersed solid method, five meshes of increasing density are compared. The volume averaged $k_L a$ value, calculated for a 1 mm constant bubble size using the eddy cell model, is used as a measure of mesh independence. For this geometry, Mesh 4 was selected as the optimal density, since further increases in the number of elements offers limited improvement in solution accuracy for the increased computational load.

Table 4: Mesh dependency study (1 mm constant bubble size).

Mesh	Number of Elements			Mass Transfer Coefficient
	Total	Stationary region	Impeller region	$k_L a$ (hr^{-1}) (Eddy cell)
1	209,555	154,294	12,320 + 42,941	56.31
2	431,914	349,794	18,144 + 63,976	54.58
3	821,909	693,064	23,400 + 105,445	60.73
4	997,828	844,316	23,400 + 130,112	62.29
5	1,548,956	1,375,456	23,400 + 150,110	62.22

3.3 Sensitivity Analysis of MUSIG Model Parameters

In order to ensure that the solution is not constrained by the specification of minimum and maximum bubble diameters in the definition of the population balance, a sensitivity study is performed. A base case of 400 RPM stirrer speed and 0.1 vvm aeration rate is used. Due to the introduction of relatively small bubbles at the inlet, and the possibility of bubble breakage close to the impeller, the minimum bubble size is fixed at 0 mm. The maximum bubble size is increased from 3 mm in 3 mm increments up to a maximum size of 12 mm, with an initial estimate of 12 groups. Figure 3 shows that the maximum bubble size is constrained by the range used for 0-3 and 0-6 mm, where the maximum bubble size in the domain is limited by the value specified in the population balance model. For the range 0-12 mm, the maximum bubble size in group 8, with a diameter of 7.5 mm, and well below the maximum specified size. This is not desirable since the individual groups will be larger, losing definition of the distribution. An optimum range of 0-9 mm is therefore selected for the MUSIG size range, to be applied to all conditions modelled, in accordance with the maximum bubble size seen in Figures c) and d).
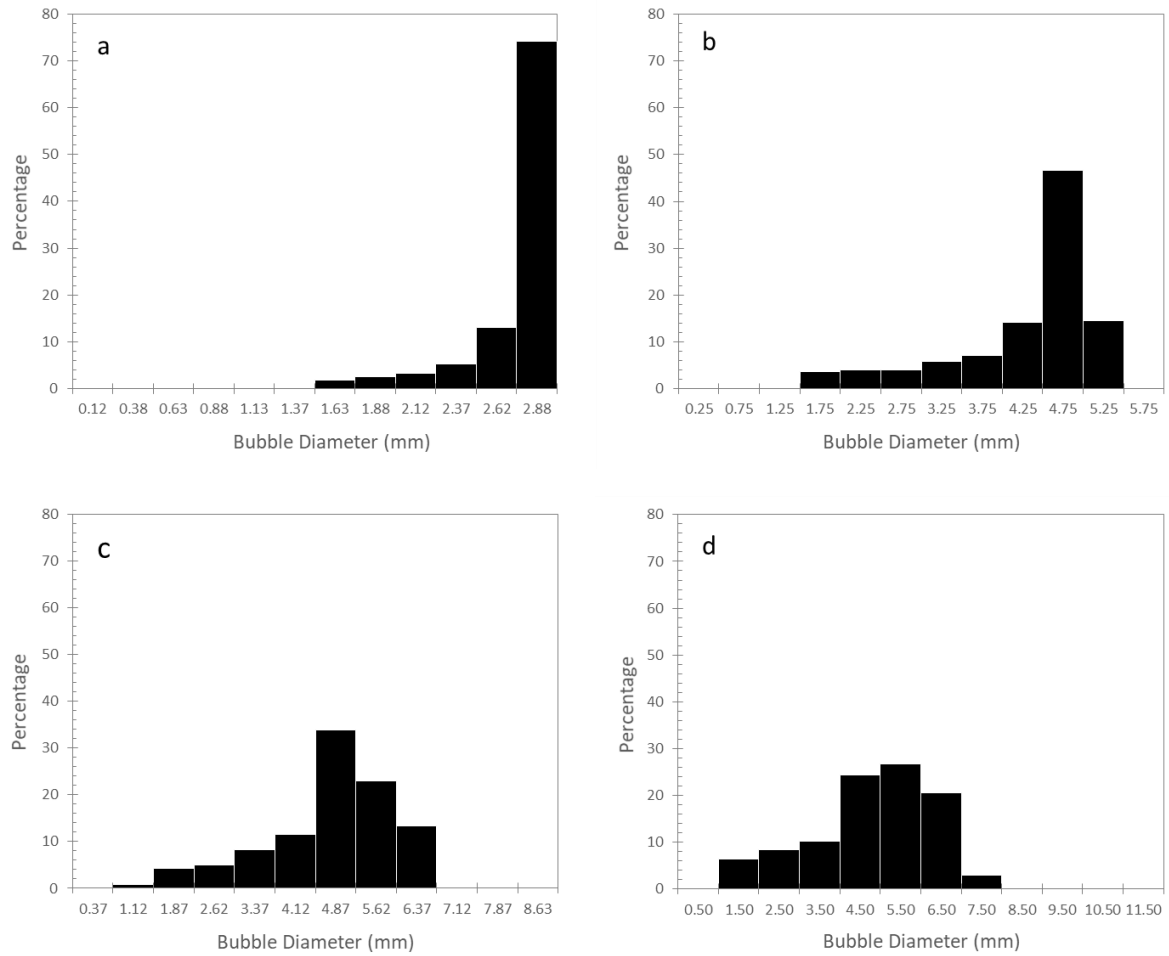
Figure 3: Bubble size distributions for different MUSIG size ranges.

a) 0-3 mm, b) 0-6, mm c) 0-9 mm, d) 0-12 mm.

A further sensitivity analysis is performed with the chosen size range by increasing the number of size groups from 12 to 24. This increases the resolution of the solution, capturing greater detail relating to the distribution and interaction between different bubble size groups, at the expense of greater computational time per iteration. Table 5 shows that there is marginal difference in the calculated volume-averaged $k_L a$ within the range specified, meaning that 12 size groups is sufficient to capture the necessary detail in the bubble size distribution to accurately model the mass transfer.

Table 5: Volume averaged $k_L a$ values using the eddy cell model for different numbers of population balance size groups (MUSIG size range 0-9 mm).

Number of Groups	Average $k_L a$ (hr^{-1}) (Eddy Cell)
12	17.6034
18	17.4400
24	17.9652

4. Results and Discussions

Vector plots of liquid velocity (Figure 4) and gas velocity (Figure 5) show the flow patterns in the SUT bioreactor at stirrer speeds from 0 to 500 RPM. At low stirrer speeds, the flow patterns are dominated by the rising gas phase, with the highest velocity for both phases at the centre of the tank. At 200 RPM, the action of the impeller becomes strong enough that there is some recirculation of the liquid phase close to the impeller, which becomes larger with increasing stirrer speed. Some recirculation of the gas phase is also seen at the highest stirrer speeds, however the predominant gas velocity occurs vertically in all cases due to the buoyant gas phase. In contrast, there is a strong recirculation of the liquid phase at the centre of the tank for speeds of 400 RPM and above, showing that the action of the impeller is able to influence the low patterns throughout the entire vessel at high stirrer speeds. The difference in flow patterns seen between the two phases is a key driver behind the interphase mixing and mass transfer for this reactor design.
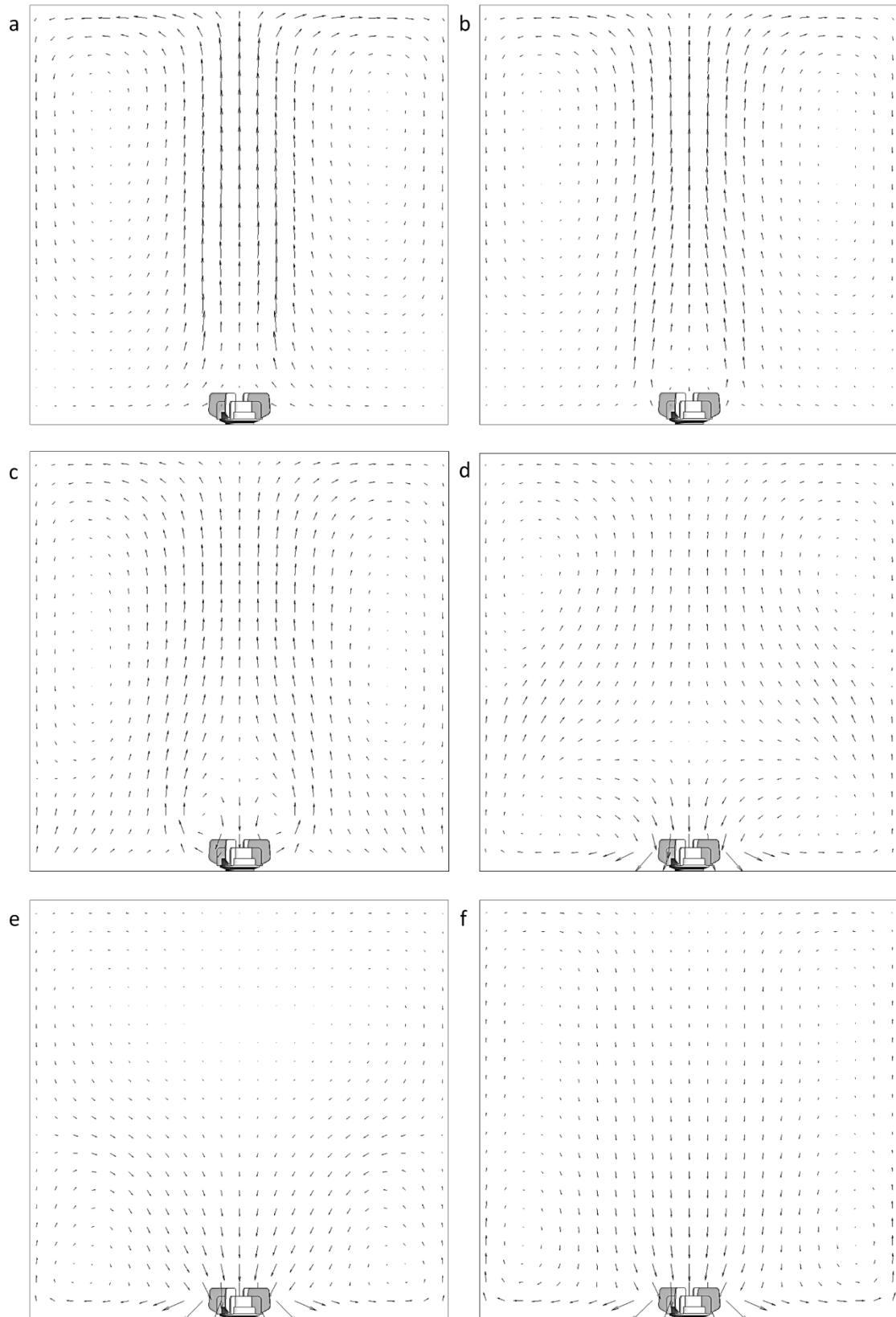
Figure 4: Liquid phase velocity vector plots at a vertical cut-plane through the centre of the SUT

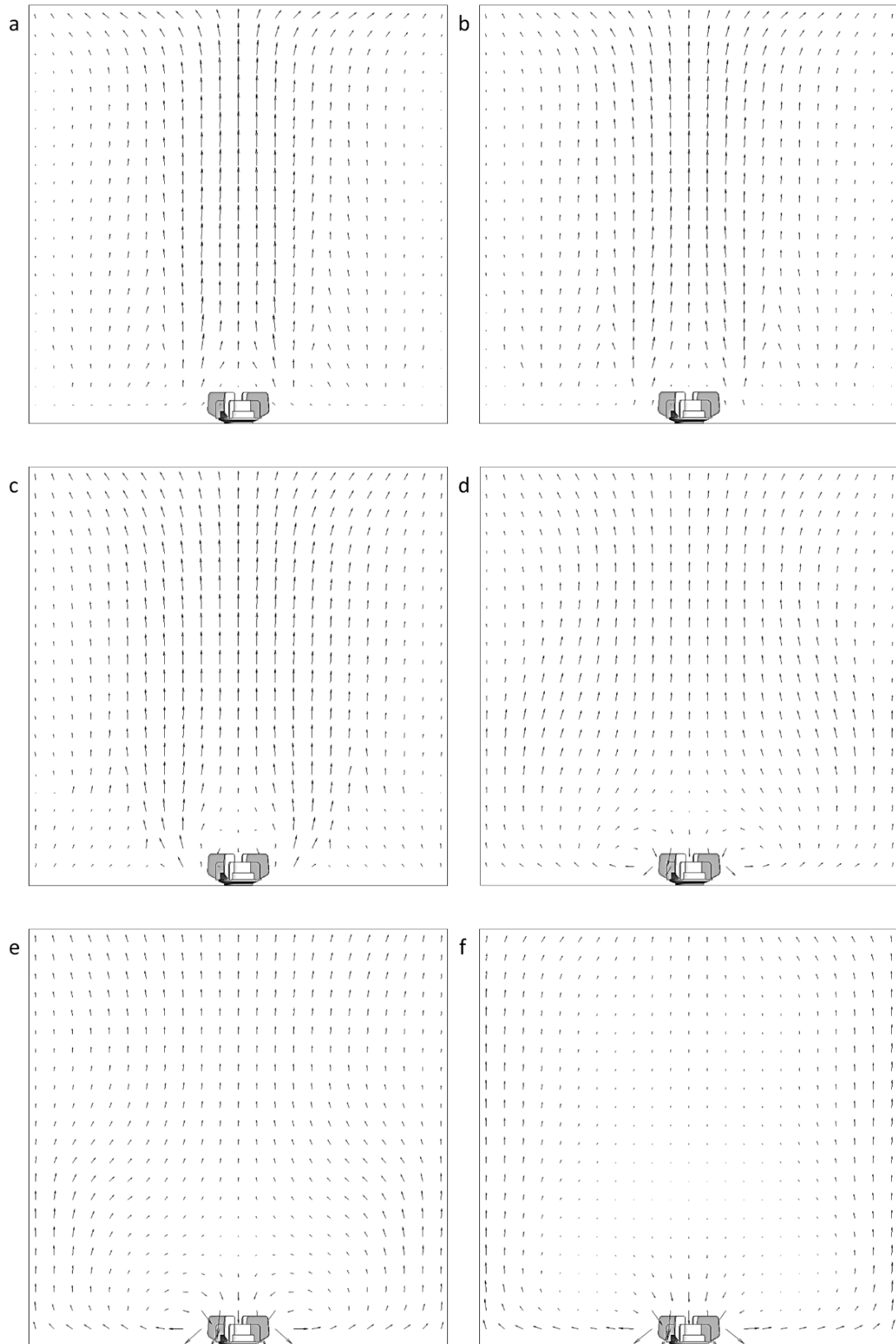bioreactor. a) 0 RPM, b) 100 RPM, c) 200 RPM, d) 300 RPM, e) 400 RPM, f) 500 RPM.

Figure 5: Gas phase velocity vector plots at a vertical cut-plane through the centre of the SUT

bioreactor. a) 0 RPM, b) 100 RPM, c) 200 RPM, d) 300 RPM, e) 400 RPM, f) 500 RPM.

Contour plots of the air fraction for a vertical cross section through the centre of the reactor is shown in Figure 6 for stirrer speeds from 0 to 500 RPM. At low speeds, the action of the impeller is not sufficient to create a large dispersion of the gas phase. This leaves large regions of the tank with no gas phase present, and therefore no mass transfer occurring. The rising column of bubbles at the centre of the tank creates a dense region of gas phase. At higher stirrer speeds, the gas distribution is significantly increased, with the dense regions of gas phase are limited to the regions directly next to the inner sparger ring. This is a result of the turbulence close to the impeller being high enough to break down the bubbles, as shown in Figure 7, and thus decreasing the rise velocity.

The geometrically averaged bubble size distribution at a height of 0.5 m (half of the filled height) is shown for increasing stirrer speeds in Figure 7. The distribution for stirrer speeds of 300 RPM and below show a minimum bubble size in group 3, the inlet bubble size, suggesting minimal bubble breakage is caused by the impeller. Furthermore, the shape of the distribution is similar between 0 and 200 RP<, showing that the impeller is having minimal influence on the bubble size at these stirrer speeds. In contrast, for higher stirrer speeds (300 RPM and above) the distribution is weighted towards the smaller bubbles, with a significant number of bubbles present in group 2, with a smaller diameter than the inlet size, as shear-induced bubble breakage becomes more significant close to the impeller.
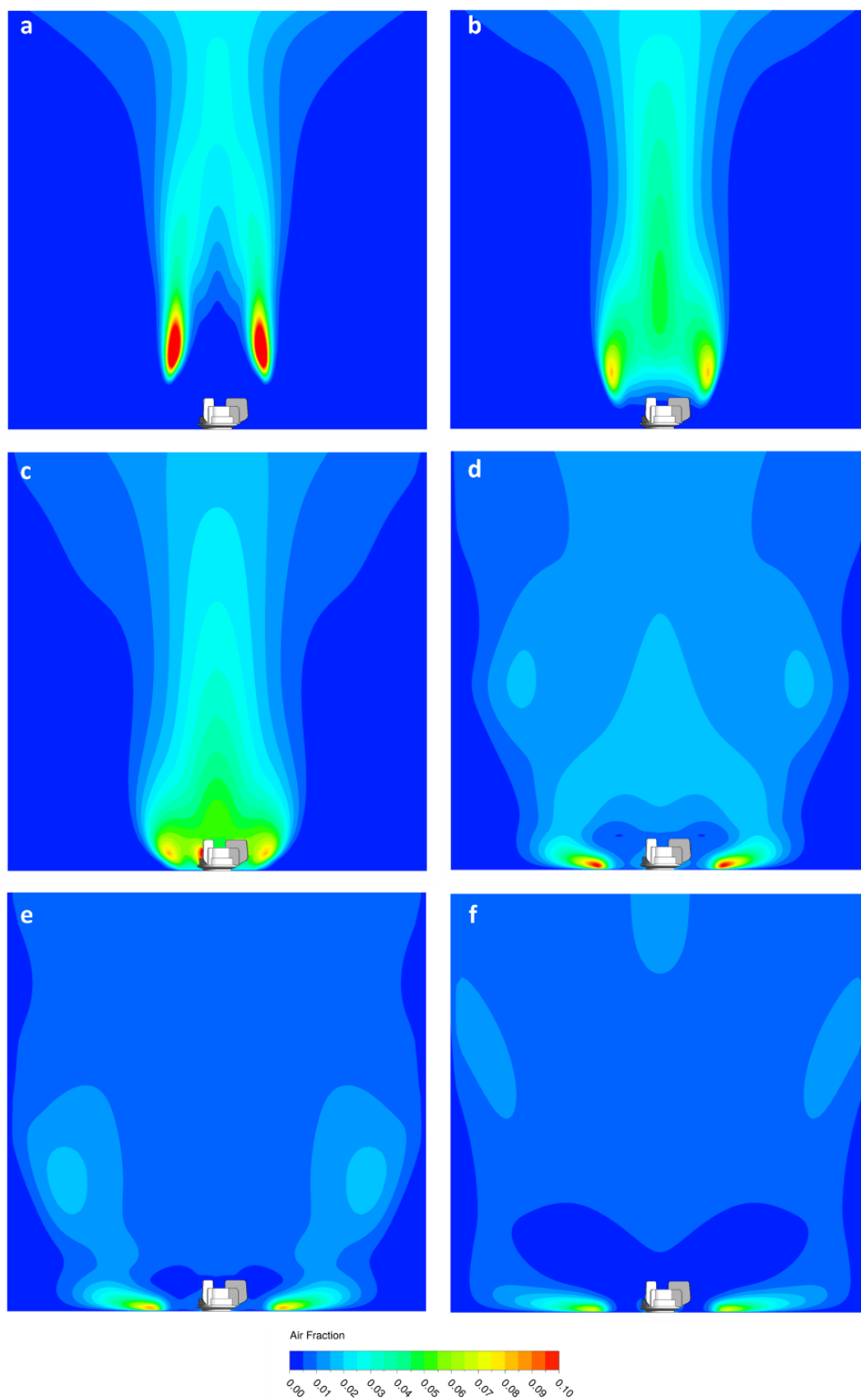
Figure 6: Contour plots of gas volume fraction at a vertical cut-plane through the centre of the SUT

bioreactor. a) 0 RPM, b) 100 RPM, c) 200 RPM, d) 300 RPM, e) 400 RPM, f) 500 RPM.
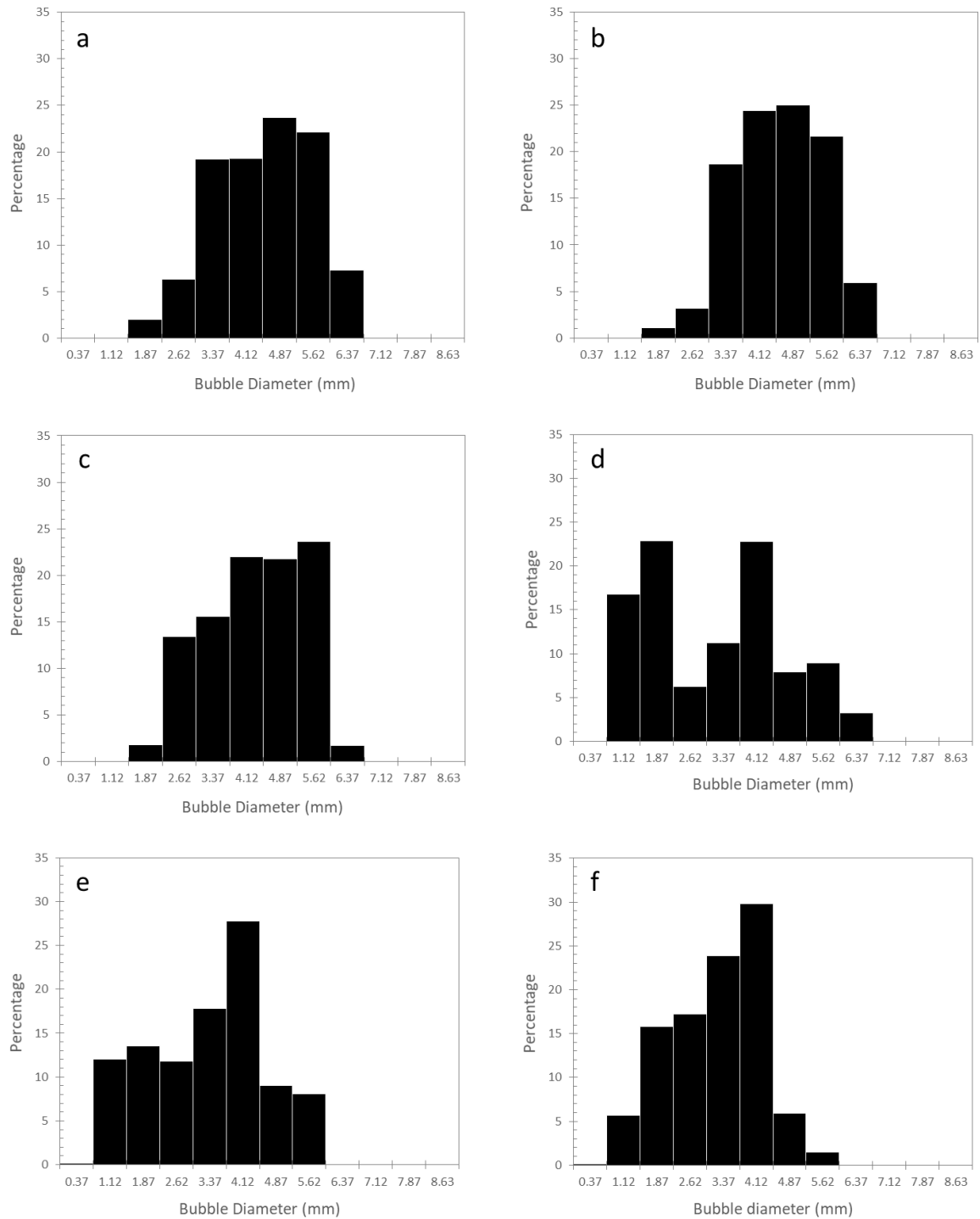
Figure 7: Bubble size distributions at a horizontal cut-plane at a height of 500 mm (50% of filled height) for different stirrer speeds, 0.1 vvm. a) 0 RPM, b) 100 RPM, c) 200 RPM, d) 300 RPM, e) 400 RPM, f) 500 RPM.

Experimental $k_L a$ values for an air-water system (provided by the Centre for Process Innovation) have been measure at multiple locations within the tank using the dynamic method. Measured $k_L a$ values varied between 35 and 40 hr^{-1} at a stirrer speed of 400 RPM. The range of $k_L a$ values predicted by the different models using the population balance (MUSIG) model under the same conditions varies significantly between the different mass transfer models, as shown in Figure 8. The slip velocity (equation 31) and surface renewal stretch (SRS) models (equation 33) both lie on the ± 20% line from the mid-point of the experimental range, with the slip velocity under-predicting and the surface renewal stretch model over-predicting the measured values. The eddy cell (equation 30) and penetration models (equation 29), which share the same form with different proportionality constants, predicted values either side of the experimental range. This suggests that a model of the form described by equation 1 may be applicable with modified constants, however the most commonly used theoretically derived constants are not able to accurately predict the mass transfer coefficient. The rigid model under-predicts the $k_L a$ by a very large amount, showing that the deformation of the bubble surface is very significant in modelling the mass transfer coefficient with bubbles in the size range presented here, as suggested by Alves *et al* [20].

From equation 4 it is clear that the bubble size also plays a significant role in the mass transfer due to the inverse dependency of the specific area on the bubble diameter. At the sparger, the bubble size is assumed uniform, however significant coalescence close to the sparger means that a distribution of bubble sizes covering larger bubble sizes is developed by a height of 0.1 m. This distribution becomes further weighted towards the larger bubble sizes as further coalescence occurs towards the top of the tank, with a low fraction of small bubbles still present when they reach the liquid surface. Unlike traditional fermenter design, which sparge the gas directly onto the impeller to promote bubble breakage, there is no mechanism for significant bubble breakage throughout the majority of this SUT design, meaning that the mass transfer rate is very non-uniform with height. It is

therefore necessary to design such equipment with sparging configurations that will minimise
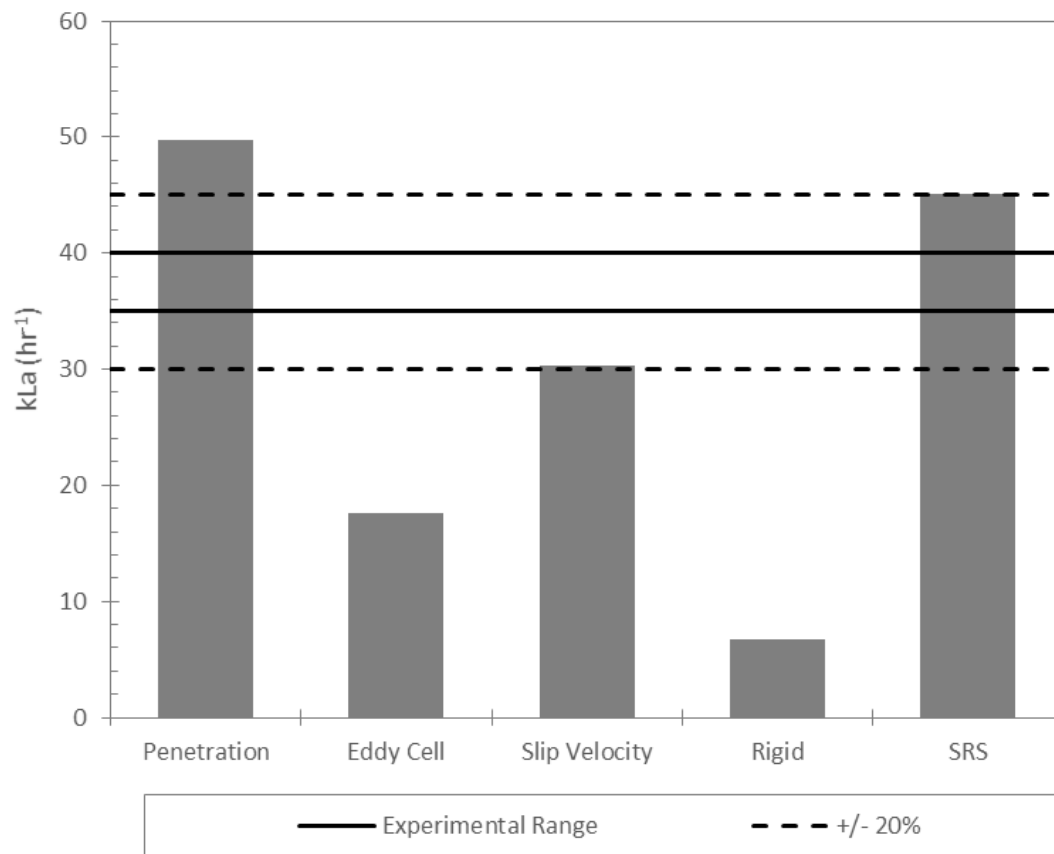
bubble coalescence.

Figure 8: Comparison of predicted $k_L a$ values using different mass transfer models and experimental

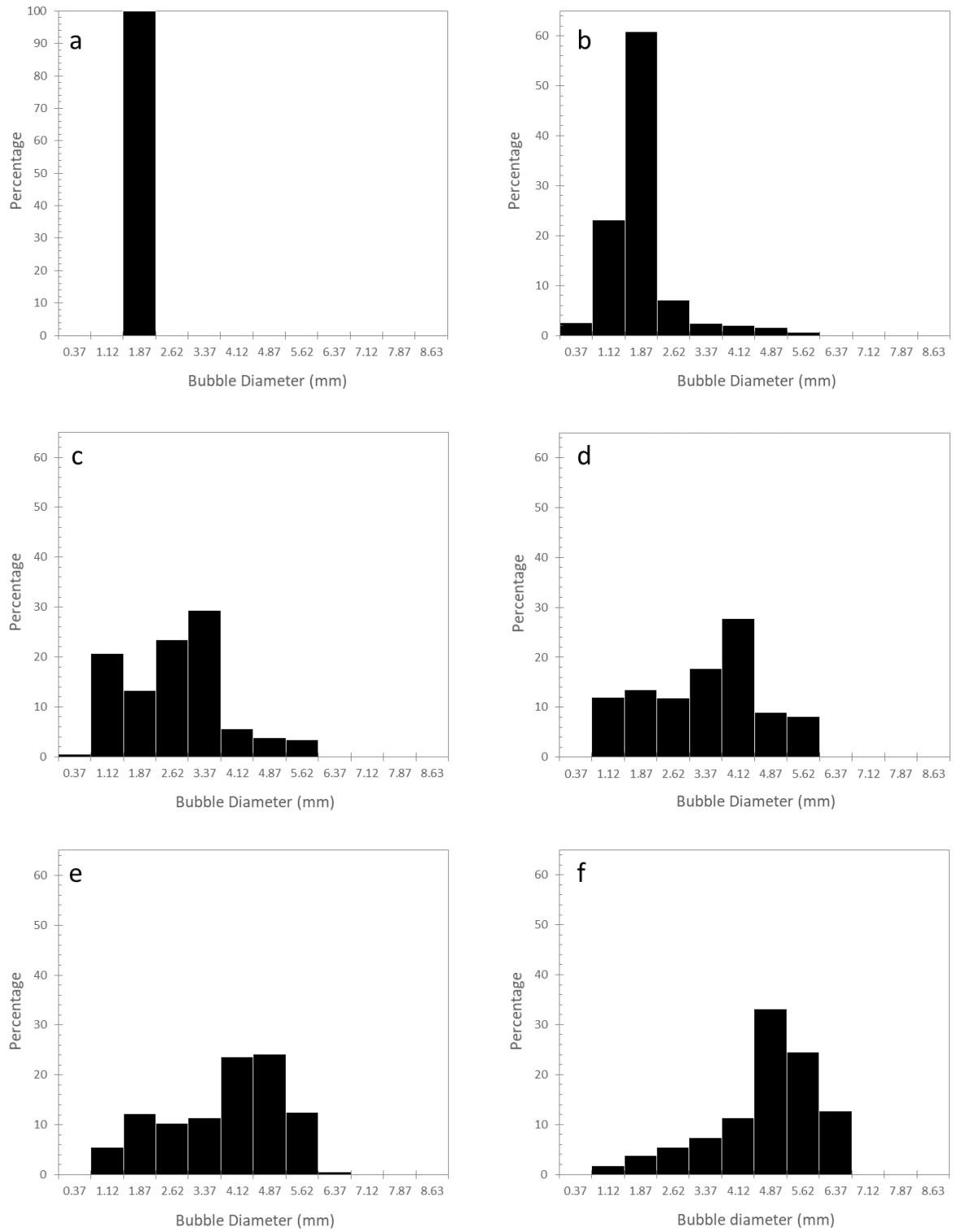measurements using the dynamic method at 400 RPM and 0.1 vvm.

Figure 9: Bubble size distributions at horizontal cut-planes of increasing height within the SUT

bioreactor at 400 RPM and 0.1 vvm.

a) Inlet, b) 100 mm, c) 250 mm, d) 500 mm, e) 750 mm, f) 1000 mm.

The turbulent kinetic energy (TKE) distributions within the liquid phase are plotted in Figure 10 over the range of stirrer speeds investigated. At 0 RPM, the highest turbulence is found close to the top surface of the liquid, where the mean liquid flow patterns are seen to rapidly change direction from vertical to horizontal. At all other conditions, the highest turbulence levels are found close to the impeller, although for the 100 RPM case the distribution of turbulence is reasonably well distributed across the plane. At stirrer speeds of 200 RPM and above, the highest region of turbulence is localised to the region immediately surrounding the impeller, with very little difference for the distributions presented for 300 RPM and above. Each individual plot is presented alongside its own colour bar due to the wide range of maximum TKE values modelled for the different stirring conditions, ranging from 0.140 $m^2 s^{-2}$ for 100 RPM to 3.78 $m^2 s^{-2}$ for 500 RPM. This means that the intensity of the turbulence increases significantly at higher stirrer speeds despite the similar distributions, contributing to the increased levels of bubble break-up predicted by the CFD model.
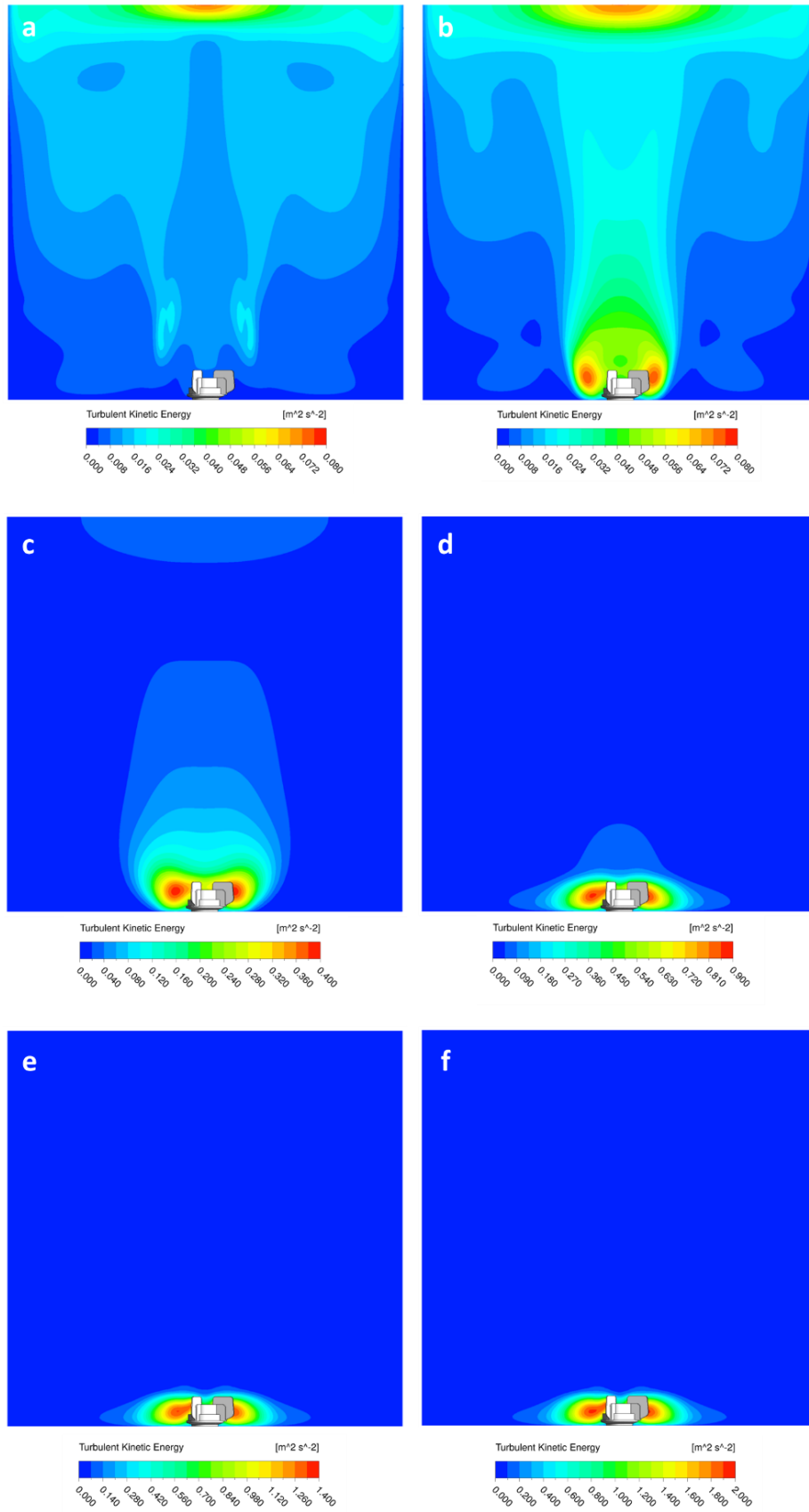
Figure 10: Contour plots of turbulent kinetic energy at a vertical cut-plane through the centre of the SUT bioreactor. a) 0 RPM, b) 100 RPM, c) 200 RPM, d) 300 RPM, e) 400 RPM, f) 500 RPM.

The volume averaged $k_L a$ values for stirrer speeds from 0 to 500 RPM – the physical limit imposed on the system to avoid impeller lift - are shown in Figure 11. The profile plotted by each model follows a similar trend, with a clear increase in $k_L a$ with stirrer speed seen across the range. This shows that despite the relatively small impeller-to-tank size ratio and distributed sparging and significant bubble coalescence towards the liquid surface, the impeller action is able to significantly improve mass transfer. The two most commonly used forms of mass transfer model, the eddy and slip velocity models show slightly different trends at 200 RPM, with the eddy cell and penetration models showing a larger increase, however the gap between the profiles remains fairly consistent across the range.
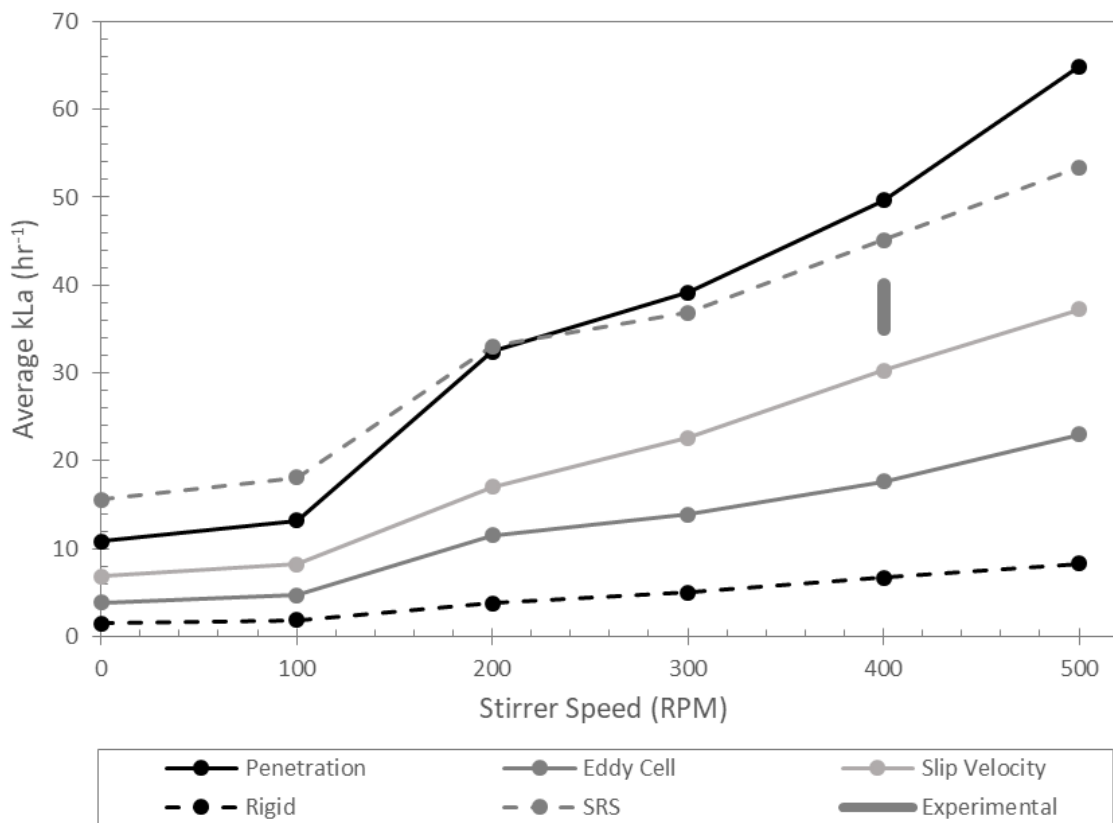

Figure 11: Comparison of volume averaged $k_L a$ for different mass transfer coefficient models at stirrer speeds from 0 to 500 RPM.

Figure 12 compares the local values of $k_L a$ and k_L at the central cut-plane of the reactor for the eddy cell and slip velocity models. The difference between the magnitude of the $k_L a$ (Figure 12a) predicted by the two models is much greater than that presented by Gimbun *et al* [24] for traditional 14 and 200 L baffled stirred tanks, where the two models gave very similar values, especially for larger vessels. Furthermore, the order of the slip velocity and eddy cell models in this study is reversed from the findings of Ranganathan and Sivaraman [23] for a multi-impeller system. Such designs have a much more even distribution of turbulence throughout the vessel, leading to higher predictions using the eddy cell model than have been predicted in this study. However, the shape of the $k_L a$ distribution is still similar between the two cases, regardless of the magnitude of the $k_L a$. This is in contrast to the k_L values presented in Figure 12b), which shows that the slip velocity predicts a higher k_L throughout the majority of the vessel. This is because the majority of the turbulent energy imparted to the liquid phase in the non-standard geometry modelled here occurs in the region close to the impeller, making this region critical to the eddy cell model. Unlike the traditional stirred tanks studied by Gimbun *et al* and others, there are large regions where the slip velocity between the two phases is more significant than the eddy dissipation, since the impeller action is confined to a small area of the reactor. Therefore, this suggests that it is necessary to include non-standard systems when evaluating different mass transfer models for stirred tanks to ensure that selected models are appropriate in multiple flow regimes.

Plotting the volume-averaged values of the volumetric mass transfer coefficient (k_L) and the specific area (a) separately across the range of stirrer speeds modelled (Figure 13) shows that increasing the specific area is much more influential on the $k_L a$ than changes in the mass transfer coefficient caused by varying stirrer speed. The slip velocity model shows more variation in mass transfer coefficient over the range of stirrer speeds modelled, specifically between 200 and 300 RPM where the biggest change in the gas distribution is seen (Figure 6). This suggests that accurately modelling the specific area, calculated from the hydrodynamics and population balance modelling, is critical in

the accurate prediction of mass transfer in stirred tanks. This also explains the use of constant k_L in some two-phase mass transfer investigations, predominantly for bubble columns where the conditions are more uniform. This analysis suggests that increasing the specific area between the two phases is the most beneficial method for improving $k_L a$ performance. It is therefore recommended that increased efforts are applied to minimising bubble size and bubble coalescence in applications where interphase mass transfer is limiting.
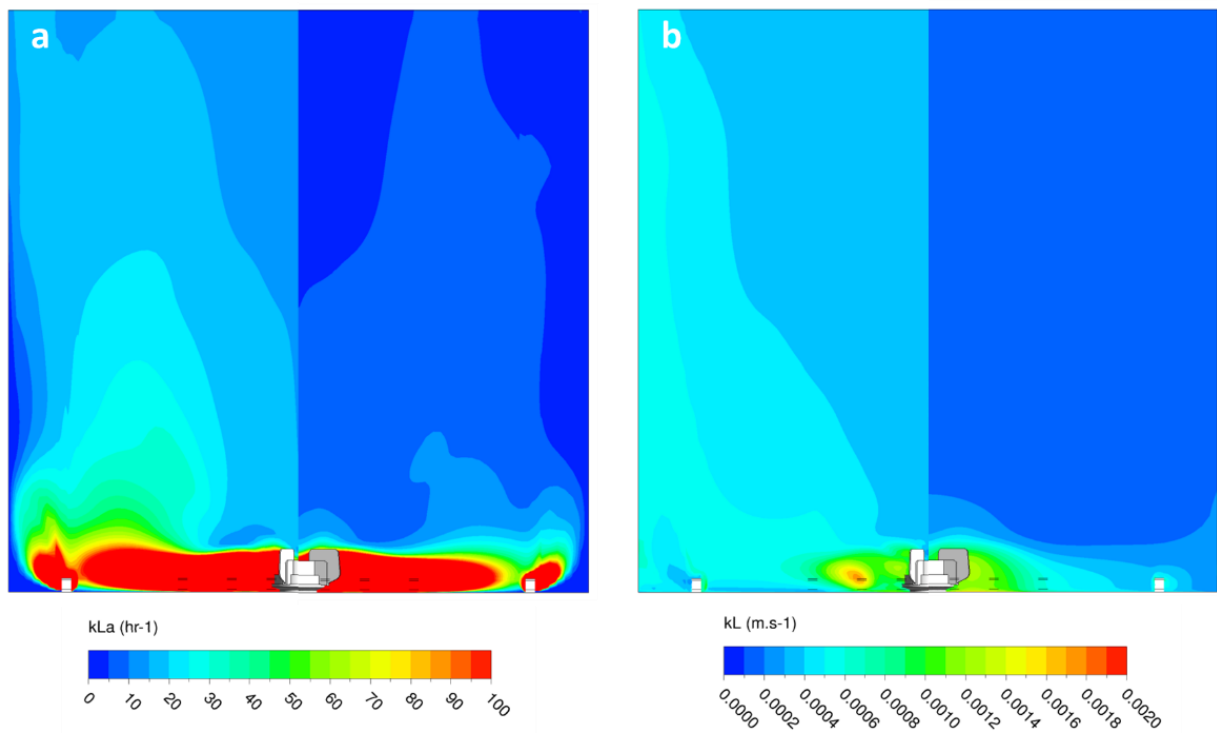

Figure 12: Comparisons between the slip velocity (left) and eddy cell (right) models at a central cut plane for a) $k_L a$ (range limited to 100 hr^{-1}), and b) k_L.

Analysis of the novel SUT bioreactor using computational fluid dynamics has shown the unique mixing and mass transfer behaviour occurring within the design. In contrast to traditional stainless steel fermenters, the influence of the impeller is much less in determining the flow patterns and bubble size distribution than in traditional designs, where the impeller action causes significant bubble break-up. However, the influence of the impeller at stirrer speeds of 400 RPM and above is

high enough to achieve good gas distribution and liquid recirculation. The magnitude of the $k_L a$ in the SUT bioreactor is lower than achieved in many stainless steel designs, however many aerobic processes can still be performed with current mass transfer performance, thus helping to expand the appeal of SUT equipment due to the reduced costs and complexity associated with the presented design. The turbulence within the reactor is found to be more localised than in traditional designs, highlighting differences between the most commonly used mass transfer models which are not apparent in typical designs, where the turbulence is much more evenly distributed.
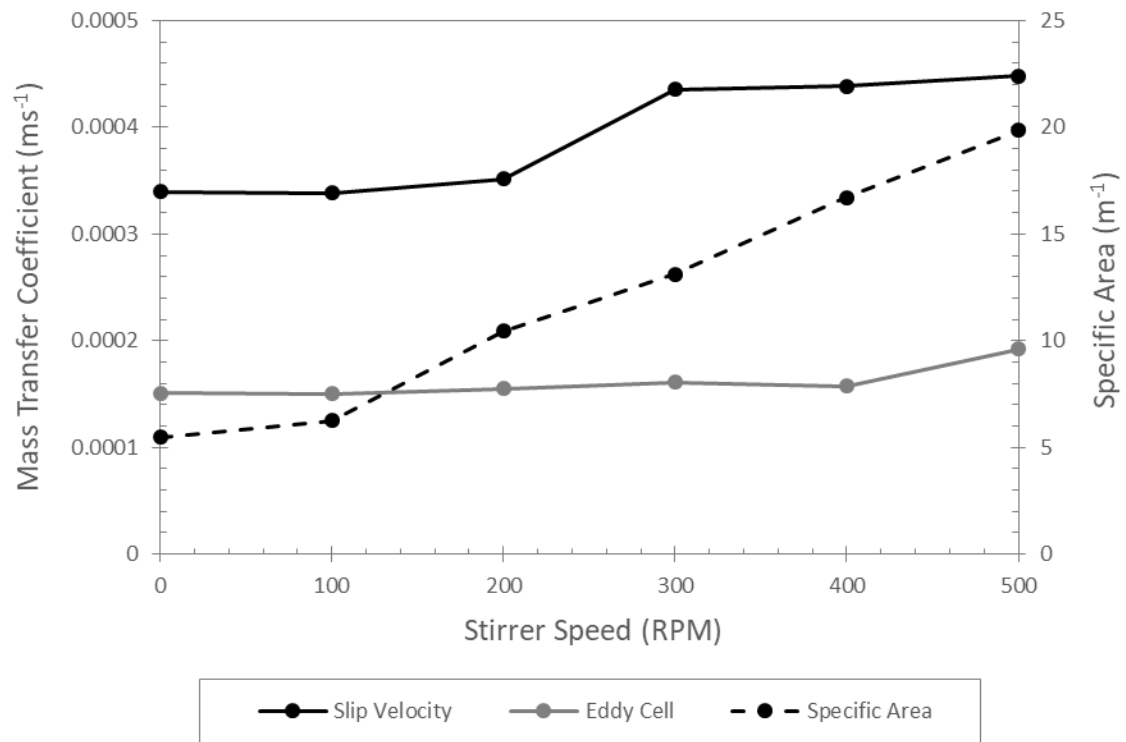

Figure 13: Comparison of k_L values for the slip velocity and eddy cell models and the specific area at stirrer speeds from 0 to 500 RPM.

Conclusions

CFD modelling has been applied to a novel 1,000 L single use technology bioreactor design, with a floor-mounted magnetically driven impeller and distributed gas sparging. Analysis of the flow patterns and bubble size distributions shows that there is significant bubble breakage occurring at stirrer speeds of 300 RPM and above, coinciding with a greater distribution of the gas phase within the reactor.

Analysis of the mass transfer thought $k_L a$ values shows that the slip velocity form of Higbie's model [14] provides the best fit to experimental data at 400 RPM out of the commonly used models identified. The surface renewal stretch model [22] also provided a reasonable fit to the available experimental data. The experimental values fall in-between the eddy cell and penetration models, which share the same form, however neither theoretically derived constant was able to sufficiently describe the volume-averaged mass transfer coefficient.

Separating the mass transfer coefficient (k_L) and specific area (a) shows that the specific area is much more significant in driving changes in $k_L a$ at different stirrer speeds for the system considered. A change in the order between the different models considered when compared to traditional stirred tank designs [23,24] shows the need to consider non-traditional designs when identifying suitable mass transfer models for different flow regimes.

Nomenclature

a = specific are (m^{-1})

C_D = drag coefficient (-)

C_{O_2} = dissolved oxygen concentration (mol m^{-3})

$C_{O_2}{}^*$ = saturation oxygen concentration (mol m^{-3})

$C_{\varepsilon 1}$ = k-ε equation constant (-)

$C_{\varepsilon 2}$ = k-ε equation constant (-)

C_μ = k-ε equation constant (-)

d_b = bubble diameter (m)

d_i = mean MUSIG group diameter (m)

d_{max} = maximum bubble diameter (m)

d_{min} = minimum bubble diameter (m)

$D_{g,l}$ = interphase drag force (N m^{-3})

D_L = mass diffusivity (m^2 s^{-1})

F^{TD} = turbulent dispersion force (N m^{-3})

$\boldsymbol{g}$ = gravitational vector

$g(m;\varepsilon)$ = specific breakup rate (s^{-1})

i = MUSIG group number (-)

k = turbulent kinetic energy (m^2 s^{-2})

k_l = volumetric mass transfer coefficient (m s^{-1})

K = proportionality constant (-)

N= number of MUSIG groups (-)

N_{O_2} = oxygen transfer rate (mol m^{-3} s^{-1})

$n(m,t)$ = number density (m^{-3})

P = pressure (Pa)

P' = modified pressure (Pa)

$Q(m;\varepsilon)$ = specific coalescence rate (m^3 s^{-1})

Re = Reynolds number (-)

Re_m = mean Reynolds number (-)

S_k = momentum source term (N m^{-3})

Sc = Schmidt number (-)

Sh = Sherwood number (-)

$\boldsymbol{u}$ = velocity vector (ms^{-1})

v = kinematic viscosity (m^2 s^{-1})

V_G = superficial gas velocity (m s^{-1})

v_b = slip velocity (m s^{-1})

α = volume fraction (-)

ε = turbulence dissipation (m^2 s^{-3})

μ = dynamic viscosity (Pa s)

μ_{eff} = effective viscosity (Pa s)

μ_T = turbulent viscosity (Pa s)

ρ = mass density (kg m^{-3})

σ_k = k-ε equation constant (-)

σ_ε = k-ε equation constant (-)

Acknowledgements

References

[1]   A.G. Lopes, Single-use in the biopharmaceutical industry: A review of current technology impact, challenges and limitations, Food Bioprod. Process. 93 (2015) 98–114.

[2]   R. Brecht, Disposable Bioreactors: Maturation into Pharmaceutical Glycoprotein Manufacturing, in: R. Eibl, D. Eibl (Eds.), Disopsable Bioreact., Springer, Heidelberg, 2009: pp. 1–32.

[3]   D. Kranjac, Validation of Bioreactors : Disposable vs Reusable, Bioprocess Int. 2 (2004) 86.

[4]   M. Pietrzykowski, W. Flanagan, V. Pizzi, A. Brown, A. Sinclair, M. Monge, An environmental life cycle assessment comparison of single-use and conventional process technology for the production of monoclonal antibodies, J. Clean. Prod. 41 (2013) 150–162.

[5]   R. Eibl, S. Kaiser, R. Lombriser, D. Eibl, Disposable bioreactors: The current state-of-the-art and recommended applications in biotechnology, Appl. Microbiol. Biotechnol. 86 (2010) 41–49.

[6]   R. Eibl, S. Werner, D. Eibl, Disposable bioreactors for plant liquid cultures at litre-scale, Eng. Life Sci. 9 (2009) 156–164.

[7]   T. Dreher, U. Husemann, C. Zahnow, D. De Wilde, T. Adams, G. Greller, High cell density escherichia coli cultivation in different single-use bioreactor systems, Chemie-Ingenieur-Technik. 85 (2013) 162–171.

[8]   P.S. Harvey, M. Greaves, Turbulent flow in an agitated vessel. Part I: A predictive model, Trans IChemE. 60 (1982) 195–200.

[9]   P.S. Harvey, M. Greaves, Turbulent flow in an agitated vessel. Part II: Numerical Solution and Model Predictions, Trans IChemE. 60 (1982) 201–210.

[10]   J.B. Joshi, N.K. Nere, C. V. Rane, B.N. Murthy, C.S. Mathpati, A.W. Patwardhan, V. V. Ranade, CFD simulation of stirred tanks: Comparison of turbulence models. Part I: Radial flow impellers, Can. J. Chem. Eng. 89 (2011) 23–82.

[11]   J.B. Joshi, N.K. Nere, C. V. Rane, B.N. Murthy, C.S. Mathpati, A.W. Patwardhan, V. V. Ranade, CFD simulation of stirred tanks: Comparison of turbulence models (Part II: Axial flow impellers, multiple impellers and multiphase dispersions), Can. J. Chem. Eng. 89 (2011) 754–816.

[12]   F. Garcia-Ochoa, E. Gomez, V.E. Santos, J.C. Merchuk, Oxygen uptake rate in microbial processes: An overview, Biochem. Eng. J. 49 (2010) 289–307.

[13]   P.M. Doran, Bioprocess Engineering Principles, Elsevier, London, 1995.

[14]   R. Higbie, The Rate of Absorbtion of a Pure Gas into a Still Liquid During Short Periods of Exposure, Trans. Am. Inst. Chem. Eng. 31 (1935) 365–389.

[15]   J.C. Lamont, D.S. Scott, An eddy cell model of mass transfer into the surface of a turbulent liquid, AIChE J. 16 (1970) 513–519.

[16]   Y. Kawase, B. Halard, M. Moo-Young, Liquid-Phase Mass Transfer Coefficients in Bioreactors, Biotechnol. Bioeng. 39 (1992) 1133–1140.

[17]   V. Linek, M. Kordač, M. Fujasová, T. Moucha, Gas-liquid mass transfer coefficient in stirred tanks interpreted through models of idealized eddy structure of turbulence in the bubble vicinity, Chem. Eng. Process. Process Intensif. 43 (2004) 1511–1517.

[18]   B.D. Prasher, G.B. Wills, Mass transfer in an agitated vessel, Ind. Eng. Chem. Process Des. Dev. 12 (1973) 351–354.

[19]   H. Appa, D.A. Deglon, C.J. Meyer, Numerical modelling of mass transfer in an autoclave, Hydrometallurgy. 147–148 (2014) 234–240.

[20]   S.S. Alves, C.I. Maia, J.M.T. Vasconcelos, Gas-liquid mass transfer coefficient in stirred tanks interpreted through bubble contamination kinetics, Chem. Eng. Process. Process Intensif. 43 (2004) 823–830.

[21]   N. Frössling, Über die Verdunstung Fallender Tropfen, Gerlands Beiträge Zur Geophys. 52 (1938) 170–216.

[22]   B. Jajuee, A. Margaritis, D. Karamanev, M. a. Bergougnou, Application of surface-renewal-stretch model for interface mass transfer, Chem. Eng. Sci. 61 (2006) 3917–3929.

[23]   P. Ranganathan, S. Sivaraman, Investigations on hydrodynamics and mass transfer in gas-liquid stirred reactor using computational fluid dynamics, Chem. Eng. Sci. 66 (2011) 3108–3124.

[24]   J. Gimbun, C.D. Rielly, Z.K. Nagy, Modelling of mass transfer in gas-liquid stirred tanks agitated by Rushton turbine and CD-6 impeller: A scale-up study, Chem. Eng. Res. Des. 87 (2009) 437–451.

[25]   A. Bakker, H.E.A. Van den Akker, A computational model for the gas-liquid flow in stirred

          reactors, Chem. Eng. Res. Des. Trans. Inst. Chem. Eng. Part A. 72 (1994) 594–606.

[26]   M. Laakkonen, V. Alopaeus, J. Aittamaa, Validation of bubble breakage, coalescence and mass

          transfer models for gas–liquid dispersion in agitated vessel, Chem. Eng. Sci. 61 (2006) 218–

          228.

[27]   F. Kerdouss, a. Bannari, P. Proulx, R. Bannari, M. Skrga, Y. Labrecque, Two-phase mass

          transfer coefficient prediction in stirred vessel with a CFD model, Comput. Chem. Eng. 32

          (2008) 1943–1955.

[28]   P. Moilanen, M. Laakkonen, O. Visuri, V. Alopaeus, J. Aittamaa, Modelling mass transfer in an

          aerated 0.2 m3 vessel agitated by Rushton, Phasejet and Combijet impellers, Chem. Eng. J.

          142 (2008) 95–108.

[29]   H. Zhang, K. Zhang, S. Fan, CFD simulation coupled with population balance equations for

          aerated stirred bioreactors, Eng. Life Sci. 9 (2009) 421–430.

[30]   A. Buffo, M. Vanni, D.L. Marchisio, Multidimensional population balance model for the

          simulation of turbulent gas-liquid systems in stirred tank reactors, Chem. Eng. Sci. 70 (2012)

          31–44.

[31]   K.M. Dhanasekharan, J. Sanyal, A. Jain, A. Haidari, A generalized approach to model oxygen

          transfer in bioreactors using population balances and computational fluid dynamics, Chem.

          Eng. Sci. 60 (2005) 213–218.

[32]   A. Cockx, Z. Do-Quang, J.M. Audic, A. Liné, M. Roustan, Global and local mass transfer

          coefficients in waste water treatment process by computational fluid dynamics, Chem. Eng.

          Process. Process Intensif. 40 (2001) 187–194.

[33]   Y. Fayolle, A. Cockx, S. Gillot, M. Roustan, A. Héduit, Oxygen transfer prediction in aeration

          tanks using CFD, Chem. Eng. Sci. 62 (2007) 7163–7171.

[34]   S. Talvy, A. Cockx, A. Liné, Modeling of oxygen mass transfer in a gas–liquid airlift reactor,

          AIChE J. 53 (2007) 316–326.

[35] T. Wang, J. Wang, Numerical simulations of gas-liquid mass transfer in bubble columns with a CFD-PBM coupled model, Chem. Eng. Sci. 62 (2007) 7107–7118.

[36] R. Krishna, J.M. Van Baten, Mass transfer in bubble columns, Catal. Today. 79–80 (2003) 67–75.

[37] D.F. Fletcher, D.D. McClure, J.M. Kavanagh, G.W. Barton, CFD simulation of industrial bubble columns: Numerical challenges and model validation successes, Appl. Math. Model. 44 (2017) 25–42.

[38] Y. Sato, K. Sekoguchi, Liquid velocity distribution in two-phase bubble flow, Int. J. Multiph. Flow. 2 (1975) 79–95.

[39] M. Ishii, N. Zuber, Drag coefficient and relative velocity in bubbly, droplet or particulate flows, AIChE J. 25 (1979) 843–855.

[40] A.D. Burns, T. Frank, I. Hamill, J.M. Shi, The Favre averaged drag model for turbulent dispersion in Eulerian multi-phase flows, 5th Int. Conf. Multiph. Flow. (2004) 1–17.

[41] ANSYS CFX-Solver Theory Guide, (2016).

[42] H. Luo, H.F. Svendsen, Theoretical Model for Drop and Bubble Breakup in Turbulent Dispersions, AIChE J. 42 (1996) 1225–1233.

[43] M.J. Prince, H.W. Blanch, Bubble coalescence and break-up in air-sparged bubble columns, AIChE J. 36 (1990) 1485–1499.